

Study on High Temperature Stability of $\text{LiNi}_{0.33}\text{Co}_{0.33}\text{Mn}_{0.33}\text{O}_2/\text{Li}_4\text{Ti}_5\text{O}_{12}$ Cells from the Safety Perspective

To cite this article: D. P. Kong *et al* 2016 *J. Electrochem. Soc.* **163** A1697

View the [article online](#) for updates and enhancements.



Study on High Temperature Stability of $\text{LiNi}_{0.33}\text{Co}_{0.33}\text{Mn}_{0.33}\text{O}_2/\text{Li}_4\text{Ti}_5\text{O}_{12}$ Cells from the Safety Perspective

D. P. Kong,^a P. Ping,^{b,z} Q. S. Wang,^{c,z} and J. H. Sun^c

^aCollege of Mechanical and Electronic Engineering, University of Petroleum of China, Qingdao 266580, People's Republic of China

^bCollege of Chemical Engineering, University of Petroleum of China, Qingdao 266580, People's Republic of China

^cState Key Laboratory of Fire Science, University of Science and Technology of China, Hefei 230026, People's Republic of China

The electrochemical and thermal stability of $\text{LiNi}_{0.33}\text{Co}_{0.33}\text{Mn}_{0.33}\text{O}_2/\text{Li}_4\text{Ti}_5\text{O}_{12}$ (LNCMO/LTO) cells at high temperature is investigated using a cycler, calorimetry analysis and X-ray diffractometry (XRD) from the safety perspective. Outstanding cycling performance and rate capability are observed for LNCMO/LTO cells at room and high temperature. The cells retain 96.9% and 95.3% capacity and more than 99% coulomb efficiency over 100 cycles under C/2 rate, and also exhibit 91.6% and 84.9% capacity retention under 5C rate, at 25 and 60°C, respectively. Detailed thermal analysis of the LNCMO/LTO cell revealed the reaction course from 50 to 300°C, which can be summarized as melting of the separator, the reaction between PF_6 and lithium intercalated in LTO, the reaction between solvents and lithium intercalated in LTO, the decomposition of LNCMO and the oxidization of solvents. The thermal analysis also indicates that the cells are thermally stable below 150°C and the greatest contribution to the heat generation is the decomposition of LNCMO and the oxidization of solvents.

© 2016 The Electrochemical Society. [DOI: [10.1149/2.1041608jes](https://doi.org/10.1149/2.1041608jes)] All rights reserved.

Manuscript submitted March 31, 2016; revised manuscript received May 13, 2016. Published June 8, 2016.

The spinel structure $\text{Li}_4\text{Ti}_5\text{O}_{12}$ (LTO) has been widely investigated as a negative electrode material for LIBs due to its high thermal stability, zero-strain insertion of lithium and lack of lithium plating with quick charging compared with the graphite negative electrode.¹⁻⁴ Batteries composed of LTO negative electrode and positive electrode such as LiMn_2O_4 (LMO), LiFePO_4 (LFPO), LiCoO_2 (LCO), $\text{LiNi}_x\text{Co}_y\text{Mn}_{1-x-y}\text{O}_2$ (LNCMO), $\text{LiNi}_{0.5}\text{Mn}_{1.5}\text{O}_4$ (LNMO) or LiMnPO_4 have longer working life and reliable cycling performances,⁵⁻¹⁰ which makes LTO a promising candidate as the negative electrode material for LIBs.

LNCMO is a widely-employed positive electrode material for LIBs.^{11,12} Compared with LMO, LFPO and LCO, LNCMO has a higher specific capacity or energy density.^{13,14} In addition, LNCMO has a better thermal stability than other positive electrode materials with higher capacity, such as LNMO.¹⁵ It is recognized that a battery system with LNCMO and LTO not only shows competitive behavior in the form of coin cells but also has an excellent balance of high-power, high-energy, low temperature, and long-life performance as a 20 Ah battery.¹⁶ These performances make the LNCMO/LTO battery attractive to the energy storage or electric vehicle application. However, studies focused on the electrochemical and thermal stability, thermodynamic and kinetic characteristics of the LNCMO/LTO system under high temperature are still rare, which are important for either thermal behavior simulation or thermal management of the battery system, and also critical to its wide application in the power plants or electric vehicles.

To evaluate the electrochemical performance of the LNCMO/LTO system under high temperature, the cycling behavior and rate capability under various charge and discharge rates at room temperature and 60°C were investigated. To clearly identify the thermal reactions within the battery under high temperature, thermal stability of the LNCMO/LTO system at elevated temperature were studied by calorimetry analysis. Based on the XRD analysis and the deconvolution study of the calorimetry test results, the detailed reaction course occurring in the LNCMO/LTO full cell and the corresponding thermodynamic and kinetic characteristics at high temperature were explored.

Experimental

$\text{Li}_4\text{Ti}_5\text{O}_{12}$ (LTO) was acquired from a commercial cell manufacturer in Shenzhen, China. $\text{LiNi}_{0.33}\text{Co}_{0.33}\text{Mn}_{0.33}\text{O}_2$ (LNCMO) was obtained from 3M Company in Shanghai, China. Organic solvents and

the electrolyte solution of 1 M LiPF_6 /ethylene carbonate (EC) + diethyl carbonate (DEC) (1:1 w/w) were purchased from Zhangjiagang Guotai-Huarong Co., Ltd. The salt LiPF_6 was produced by Tianjin Jinniu Co., Ltd. Both LTO and LNCMO electrodes were coated on Al foils with a weight ratio of active material, conductive acetylene black and polyvinylidene fluoride (PVDF) binder of 92:4:4. All electrodes were dried for 12 h in vacuum at 70°C. Coin cells were assembled in an argon-filled glove box using LTO and LNCMO electrodes as the negative and positive electrodes, respectively, with 1 M LiPF_6 /EC+DEC electrolyte solution and Celgard 2325 separators. For the half-cell measurements, lithium metal foil was employed as the negative electrode. Before assembling the full cells, the mass of each component was recorded to ensure the matching of the capacity for the electrodes and the accuracy of the thermal analysis on the full cells.

After assembly, the LNCMO and LTO half cells and LNCMO/LTO full cells were cycled 100 times at 25 and 60°C on a multi-channel battery cycler (Neware BTS2300, Shenzhen) at C/2 rate within 3.0~4.2 V, 1.2~2.8 V and 1.5~2.8 V, respectively, to study the cycling performance of the cells. The LNCMO/LTO full cells were cycled at 25 and 60°C from 1.5 to 2.8 V under various cycling rates: C/5, 1C, 5C and then C/5 back again, over 30 cycles for each rate, respectively, to characterize the rate capability of the full cells.

The C80 micro-calorimeter was employed in this work to investigate the thermal behaviors of the LNCMO/LTO system under high temperature. The C80 micro-calorimeter (SETARAM Instrumentation) belongs to the CALVET calorimeters family distinguished by their accurate and reproducible calorimetric measurements. Compared with DSC, the C80 micro-calorimeter provides the real-time change of heat flow with high sensitivity ($\geq 0.1 \mu\text{W}$) and can work with much larger sample mass (up to 10 g). Furthermore, precise detection of both exothermic and endothermic effects can be obtained by C80, which is quite different from ARC. As shown in Figure 1, the C80 is composed of two identical wells surrounded by identical fluxmeters. The fluxmeters are connected in opposition to provide a differential thermopile output, which can compensate for the effect of the environment on the measurements. The sample vessel fits closely to one of the wells and a reference vessel sits in the other well. As shown in Figure 1, the vessels are totally surrounded by 3D CALVET sensors, which are composed of 9 concentric rings, containing 38 thermocouples for each ring (342 in total), and then all heat evolved is measured. In particular, the high pressure vessel (8.5 ml) used for C80 as shown in Figure 2, is able to contain more amounts of sample than the DSC, and also can be sealed under high pressure (up to 100 bar). In this study, the sample was put into the high pressure vessel and then was sealed in the glove box to prevent the contamination of air and water.

^zE-mail: pingping@upc.edu.cn; pinew@upc.edu.cn

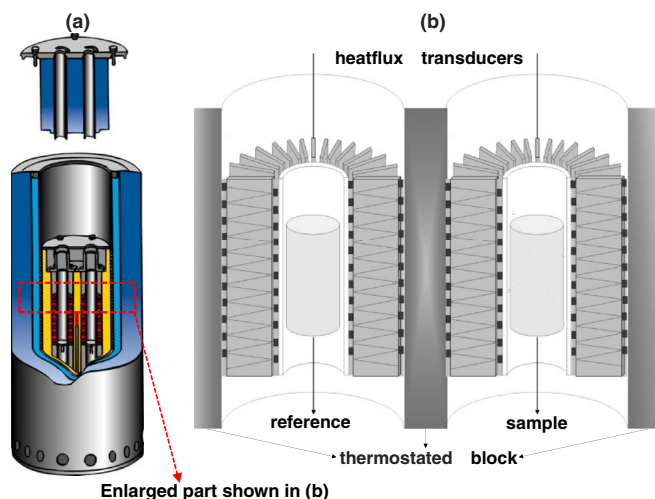


Figure 1. Schematic diagram of the C80 micro-calorimeter (a) and the enlarged part of the core component of the C80 (b).

By using a fixed base and a torque wrench ($35 \text{ N} \cdot \text{m}$), the vessel can be well sealed with high pressure (100 bar), and was then taken out from the glove box. The mass of the vessel with sample was tested before and after the C80 measurement. The similar mass values show good sealing performance of the high pressure vessel which can prevent the possible leak of samples. The isothermal and scanning technology of C80 presents heat measurements performed at constant temperature, and during a temperature program, respectively.

To obtain samples for calorimetry or XRD measurement, the LNCMO/LTO full cells, LNCMO and LTO half cells were cycled three times on the cycler at C/10 rate within 1.5~2.8 V, 3.0~4.2 V and 1.2~2.8 V, respectively, followed by charged to 2.8 V, 4.2 V or discharged to 1.2 V at C/20 rate. After the upper cutoff voltage was obtained, cells were disassembled in the glove box, and then the electrode or cell core, which would be measured by calorimetry or XRD, was taken out from the cells carefully. To obtain the required pure electrode with a specific mass, dimethyl carbonate (DMC) was used to rinse the electrode. After drying the electrode to remove DMC, the electrode materials were scraped from the Al foil. The dried electrode material and the electrolyte with specific mass (described in section Electrochemical performance of LNCMO/LTO cell) were eventually added to the C80 high-pressure vessel to perform the thermal analysis test. The required full cell for the thermal test was prepared in the form of the cell core, which was folded carefully using insulated forceps and

then put into a sample holder. The mass of the disassembled cell shell was compared to the value recorded previously, and the difference was determined as the amount of the electrolyte attached on the cell shell. The same mass of the electrolyte was then added into the cell core to ensure that all of the components in the cell shell were transferred into the sample holder. All of the preparations were conducted in the argon-filled glove box. Detailed information regarding sample preparation for the measurement by the C80 micro-calorimeter can be found in our previous work.¹⁷

After the addition of the sample, the high-pressure vessel was sealed in an argon atmosphere, and then the C80 test was performed from 50.0 to 300.0°C (or other certain temperatures) with a heating rate of $0.2^\circ\text{C min}^{-1}$. By employing the deconvolution analysis, the thermal behavior of the sample under elevated temperature can be determined as various thermal processes, which are manifested by different non-overlapping thermal peaks in the heat flow curves. To investigate reactions occurring in a particular process, the calorimetric measurement will be stopped at the end of the process with specific temperature, by using the programmable scanning and isothermal utility of the C80. For instance, if the temperature range of a thermal process is identified as 100~200°C, the programmable scanning mode can be set as stopping at 200°C with a heating rate of $0.2^\circ\text{C min}^{-1}$. After stopping the scanning mode, a half-an-hour isothermal mode is employed to keep the temperature as 200°C to prevent the thermal inertia effect of the instrument. The sample vessel is then taken out from the C80 and will be opened in the glove box by using a torque wrench and a fixed base. In this way, the heat flow curve and the product of the sample in a specific temperature range can be obtained.

XRD (Philips X'Pert Pro Super, Cu K α radiation) was used to determine the difference in the structure of the electrodes before and after the calorimetry measurement. Samples were obtained from the charged LNCMO half-cell, the discharged LTO half-cell or the products of the calorimetry measurements stopped at specific temperatures. To prevent the possible contamination of air or water for the XRD samples, an air-sensitive sample holder is used, which is composed of a plate and a semi-circular frame. The holder can be sealed with a layer of aluminized mylar shroud in the glove box to prevent air exposure. Details of the air-sensitive sample holder can be found in the following Reference 18. Diffraction patterns were collected at room temperature over a scattering angle range of 10~80°.

Results and Discussion

Electrochemical performance of half-cell.—Figures 3a, 3b shows the specific capacity and coulomb efficiency (CE) plotted versus cycle number for LNCMO/Li half-cells cycled under a C/2 rate at 25 and 60°C. Figures 3c, 3d shows the voltage versus specific capacity for the 2nd, 20th, 40th, 60th, 80th and 100th cycles for LNCMO/Li half-cells cycled under a C/2 rate at 25 and 60°C, respectively. Good capacity retention is observed for the LNCMO/Li cell at room temperature, and it exhibited a discharge specific capacity 155.8 mAh g^{-1} with 98.8% capacity retention and more than 99.6% CE after 100 cycles at a C/2 rate. At temperature up to 60°C, the cell also maintained its capacity well, with only a 2.4% loss and still more than 99.6% CE after 100 cycles. In particular, the discharge specific capacity after 100 cycles was 159.1 mAh g^{-1} at 60°C, which is slightly higher than that of the cell at room temperature. This result is possibly due to the increased ionic conductivity and lithium ion diffusivity of the electrolyte resulting in decreased electrolyte and charge transfer resistance at the higher temperature.

Figures 3e, 3f shows the specific capacity and CE plotted versus cycle number for LTO/Li half cells cycled under a C/2 rate at 25 and 60°C. Figures 3g, 3h shows the voltage versus specific capacity for selected cycles for LNCMO/Li half-cells cycled under a C/2 rate at 25 and 60°C, respectively. At 25°C, the LTO/Li cell presented a consistent reversible discharge capacity 160.2 mAh g^{-1} over 100 cycles with excellent CE and capacity retention, which were 99.8% and 99.3%, respectively. This result is attributed to the zero-strain insertion of lithium for LTO. At higher temperature, although the CE

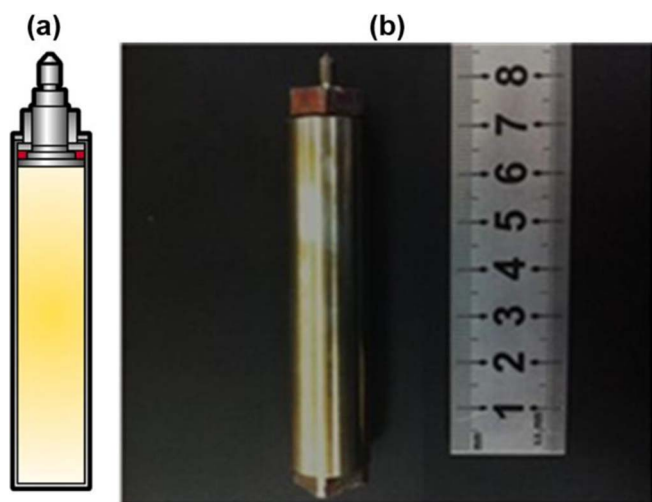


Figure 2. Schematic diagram (a) and picture (b) of the high pressure vessel.

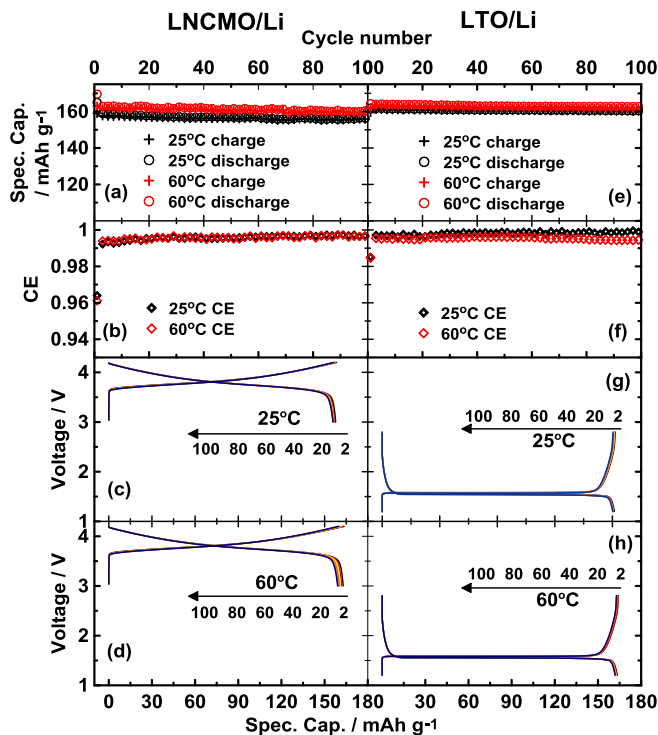


Figure 3. Specific capacity (a) and coulombic efficiency (b) versus cycle number, and voltage versus specific capacity (c, d) for the LNCMO/Li cycled under a C/2 rate at 25 and 60°C over 100 cycles. Specific capacity (e) and coulombic efficiency (f) versus cycle number, and voltage versus specific capacity (g, h) for the LTO/Li cycled under a C/2 rate at 25 and 60°C over 100 cycles.

and capacity retention fell marginally to 99.4% and 99.0% after 100 cycles, respectively, the LTO/Li cell still exhibited a consistent reversible discharge capacity 161.8 mAh g^{-1} . In light of the remarkable cycling performance of the LNCMO/Li and LTO/Li half cells at room and high temperature, further investigation into the electrochemical and thermal stability of the LNCMO/LTO full cell at high temperature was pursued in the following work.

Electrochemical performance of LNCMO/LTO cell.—Figures 4a, 4d shows the charge and discharge capacities and CE plotted versus the cycle number for the LNCMO/LTO cells cycled under C/2 rate at 25 and 60°C, respectively. Figures 4b, 4c shows the voltage versus specific capacity for selected cycles for LNCMO/LTO cells cycled under a C/2 rate at 25 and 60°C, respectively. The discharge and charge voltage for the LNCMO/LTO cell during a C/2 rate cycling was between 1.5 V and 2.8 V. A 2.5 V full cell is obtained using LNCMO and LTO as the positive and negative electrodes. The capacities of the LNMO and LTO electrodes were 2.0 and 1.9 mAh, respectively. Thus, LTO-limited LNCMO/LTO full cells were analyzed in this work. By comparison with half cells, the CEs of the full cells decreased by various extents. The CEs of the full cells increased with the cycle number and were over 99% until the 40th and 60th cycles at 25 and 60°C, respectively. The discharge capacities of the full cells cycled at 25 and 60°C over 100 cycles were similar. The differences between the full cells cycled at different temperatures are the CE and capacity retention. As shown in Figures 4a, 4d, higher CE (99.9%) and capacity retention (96.9%) over 100 cycles were observed for the full cell cycled at room temperature. The full cell cycled at 60°C still exhibited 99.1% CE and 95.3% capacity retention after 100 cycles.

Figure 4e shows the discharge capacity versus cycle number for the LNCMO/LTO cells at 25 and 60°C cycled under various cycling rates. The figure reveals excellent rate capability for the LNCMO/LTO cell at 25°C, where the cell showed 99.8%, 97.5%, 91.6% and back

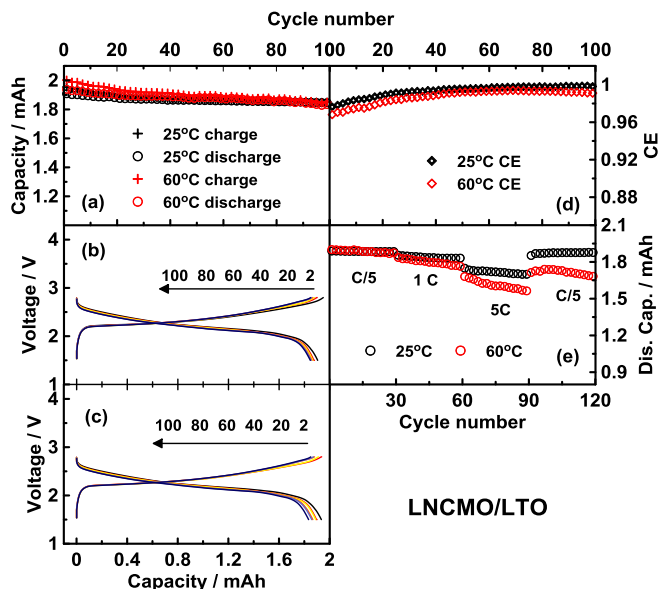


Figure 4. Capacity (a) and coulombic efficiency (d) versus cycle number, and voltage versus capacity (b, c) for the LNCMO/LTO cells cycled under a C/2 rate at 25 and 60°C over 100 cycles. Discharge capacity (e) versus cycle number for the LNCMO/LTO cells cycled under various cycling rates at 25 and 60°C.

to 99.4% capacity retention under C/5, 1C, 5C and C/5 cycling rates over 30 cycles for each rate, respectively, compared with the initial discharge capacity obtained under the C/5 rate. For each cycling rate, no obvious capacity fading was found. The capacity of the full cell cycled at 60°C resembled the cell at 25°C under the C/5 and 1C rates during the first 40 cycles. However, capacity fading is observed in the case of 5C rate. In contrast with the first cycle under a 5C rate, a 6.0% capacity loss over 30 cycles was determined. The cell at the 30th cycle under a 5C rate retained 84.9% of the first discharge capacity under a C/5 rate. For the last 30 cycles, when the cycling rate was back to C/5, the capacity was not completely back to the previous level as the cell in 25°C. Nevertheless, the capacity retention was still 90.7% compared with the capacity during the first 30 cycles under C/5.

Thermal behavior of LNCMO with the electrolyte.—To initiate the thermal analysis on the LNCMO/LTO cell, the thermal reactivity of LNCMO or LTO with and without the electrolyte was investigated first. Based on the electrode mass, the constant current and the time of current flow, the amount of the lithium deintercalated for charged (4.2 V, C/20 rate) LNCMO and the lithium intercalated for discharged (1.2 V, C/20 rate) LTO can be calculated. Then, the electrode was determined as $\text{Li}_{0.41}(\text{Ni}_{0.33}\text{Co}_{0.33}\text{Mn}_{0.33})\text{O}_2$ or $\text{Li}_{6.9}\text{Ti}_5\text{O}_{12}$, which is abbreviated as $\text{Li}_{0.41}\text{NCMO}$ or $\text{Li}_{6.9}\text{TO}$, respectively.

Figure 5i shows the heat flow versus temperature for the coexisting system of $\text{Li}_{0.41}\text{NCMO}$ (129.4 mg) and electrolyte (63.7 mg), and the separate $\text{Li}_{0.41}\text{NCMO}$ (128.8 mg) or electrolyte (63.4 mg) at high temperature. The exothermic process of single $\text{Li}_{0.41}\text{NCMO}$ was insignificant and is similar to that reported in Ref. 19. This illustrates $\text{Li}_{0.41}\text{NCMO}$ is almost thermally stable within 50.0~300.0°C. In the presence of the electrolyte, the electrode was still stable below 155.0°C. As the temperature increasing, the system displayed two exothermic process, with heat generation of -732.7 J g^{-1} , which is similar to the heat obtained in Ref. 19.

To obtain detailed information regarding the thermal behavior of $\text{Li}_{0.41}\text{NCMO}$ in the presence of the electrolyte, a deconvolution method proposed by our previous work¹⁷ was used here. Figure 5i shows the initial and the corresponding deconvoluted heat flow plots. By using the deconvolution method, two exothermic peaks P1 and P2 were picked from the plots as shown in Figure 5ii. The two peaks indicate that the thermal reaction of $\text{Li}_{0.41}\text{NCMO}$ in the electrolyte

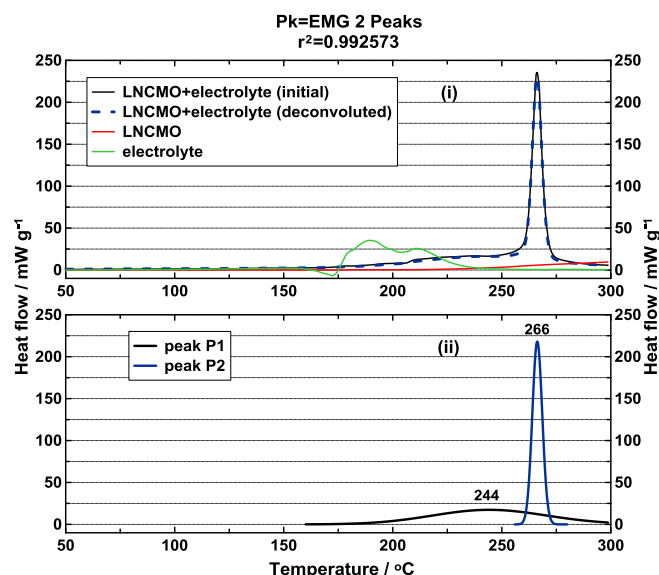
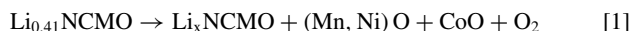


Figure 5. Heat flow versus temperature for the Li_{0.41}NCMO, the 1.0 M LiPF₆/EC + DEC electrolyte, the Li_{0.41}NCMO-electrolyte coexisting system (i) and the corresponding thermal peaks obtained from the deconvolution analysis (ii).

contains two processes, one from 160 to 255°C and the other one from 260 to 280°C. Compared with the heat flow curve of Li_{0.41}NCMO or the electrolyte in Figure 5i, the first mild exothermic process is mainly attributed to the thermal reaction of the salt LiPF₆ and the solvent EC and DEC, and probably also caused by the thermal decomposition of Li_{0.41}NCMO. To confirm if the electrode decomposed during this process, XRD analysis was conducted. Figure 6 shows the XRD diffraction pattern of the products from the coexisting system in calorimetry tests stopped at 255°C in panel (i) or 300°C in panel (ii). The XRD pattern of Li_{0.41}NCMO before the calorimetry tests is shown in panel (iii) for comparison. Figure 6i and Figure 6iii reveal the main products from the coexisting system below 260°C are LiF and Li_xNCMO, with a minor amount of (Ni,Mn)O-type and CoO phase. LiF is generated from the decomposition of LiPF₆. The reduced intensity of LNCMO diffraction lines and the appearance of (Ni,Mn)O-type and CoO imply that Li_{0.41}NCMO has experienced partial decomposition below 260°C in the presence of the electrolyte, accompanying the oxygen release, with the heat generation of 308.9 J g⁻¹, according to:



The above investigation agrees with the research conducted by Röder et al.²⁰ With the temperature increase, the Li_{0.41}NCMO electrode may become completely decomposed, and the released oxygen reacts violently with the solvents, according to:

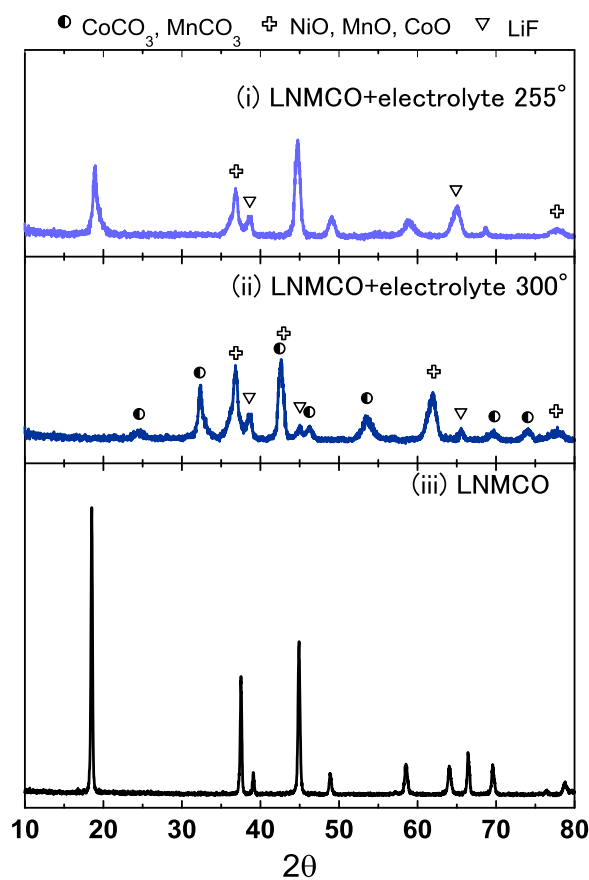
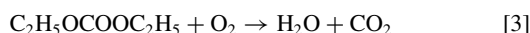
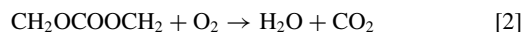
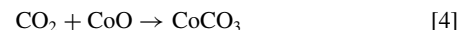


Figure 6. XRD pattern of the Li_{0.41}NCMO-electrolyte coexisting system in C80 high temperature measurements stopped at 255°C (i) and 300°C (ii). Panel (iii) displays the XRD pattern of Li_{0.41}NCMO before the high temperature measurements.

The oxidation reactions of the solvents generate CO₂ and a great deal of heat, 395.7 J g⁻¹, and contributed to the sharp peak P2 shown in Figure 5ii. The above speculation can be confirmed by XRD results shown in Figure 6ii, where LiF, CoCO₃, MnCO₃, (Ni, Mn)O-type and CoO phase were found but without Li_xNCMO in the products obtained from the thermal test at 300°C. The metal oxides react with CO₂ generated from the oxidation reaction to form MnCO₃ and CoCO₃ during the cooling process,²⁰ according to:



Based on above analysis and the method proposed in our previous work,¹⁷ the thermodynamic and kinetic parameters of the corresponding deconvoluted peaks were summarized in Table I. These parameters can be useful for the analysis of the complex thermal behavior of full

Table I. Thermodynamics and kinetics of Li_{0.41}NCMO and 1.0 M LiPF₆/EC + DEC electrolyte at 2:1 mass ratio from 50.0 to 300.0°C.

Li _{0.41} NCMO-electrolyte 2:1	Associated reaction	Onset temp. (°C)	Peak temp. (°C)	Heat (J g ⁻¹)	Activation energy E (kJ mol ⁻¹)	pre-exponential factor A (s ⁻¹)	Relativity R ²
Peak P1	reaction of salt and solvents, partial decomposition of LNCMO	160.2	244.1	-308.9	176.9	5.8 × 10 ¹⁴	0.996
Peak P2	complete decomposition of LNCMO, oxidization of solvents	256.8	266.2	-395.7	512.2	5.5 × 10 ¹²⁴	0.985
Total		-	-	-704.6	-	-	-

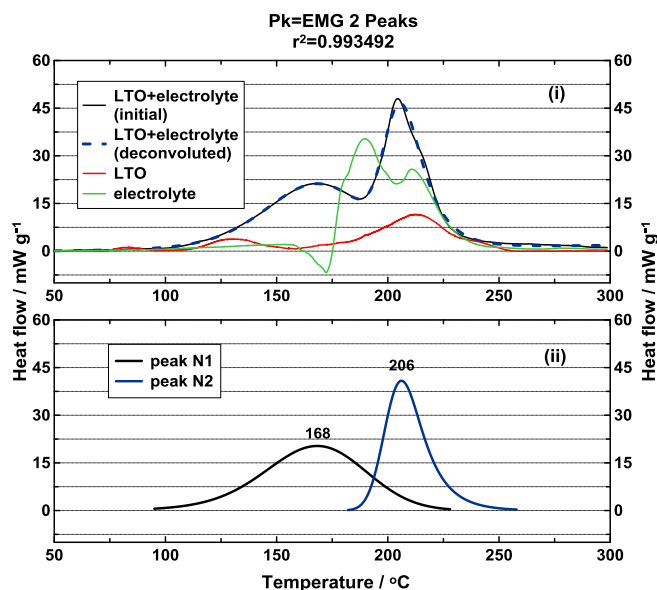
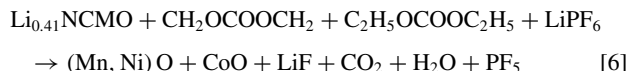


Figure 7. Heat flow versus temperature for the $\text{Li}_{6.9}\text{TO}$, the 1.0 M $\text{LiPF}_6/\text{EC} + \text{DEC}$ electrolyte, the $\text{Li}_{6.9}\text{TO}$ -electrolyte coexisting system (i) and the corresponding thermal peaks obtained from the deconvolution analysis (ii).

cell. Furthermore, the following overall thermal reactions can be assumed for the $\text{Li}_{0.41}\text{NCMO}$ in the presence of the electrolyte at high temperature:



Thermal behavior of LTO with the electrolyte.—Figure 7i shows the heat flow plots of the coexisting system of $\text{Li}_{6.9}\text{TO}$ (118.5 mg) and electrolyte (58.1 mg), and the separate $\text{Li}_{6.9}\text{TO}$ (120.6 mg) or electrolyte (59.7 mg) at high temperature. The single $\text{Li}_{6.9}\text{TO}$ began to release heat slightly within 110 ~ 150°C and then was stable until 170°C. After that, it exhibited an exothermic peak with a peak temperature 210°C. With the addition of the electrolyte, the electrode showed an increased heat flow and very different thermal behavior by comparison with the single electrode or electrolyte.

From the deconvolution analysis, exothermic peaks N1 and N2 were found for the thermal behavior of the coexisting system, as shown in Figure 7ii. The two peaks started around 100 and 185°C, and reached maxima at 168.2 and 206.2°C, with heat generation of 306.8 and 269.4 J g^{-1} , respectively. Figure 8 shows the XRD diffraction pattern of the products from the coexisting system in calorimetry tests stopped at 185°C in panel (i) or 300°C in panel (ii). The XRD pattern of $\text{Li}_{6.9}\text{TO}$ at room temperature is shown in panel (iii) for comparison. The results illustrate that the structure of LTO is stable even in the presence of the electrolyte, at either 185 or 300°C. LTO and LiF phases were detected clearly both in Figure 8i and Figure 8ii. However, Li_2CO_3 was only found in Figure 8ii. LiF is believed to arise from the decomposition of LiPF_6 , and the reaction of PF_5 with

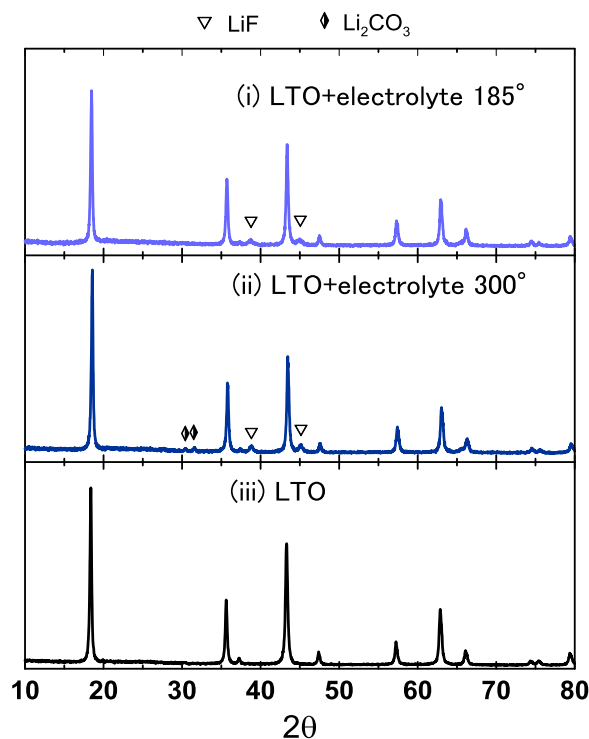
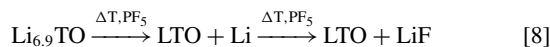
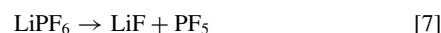
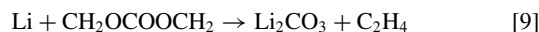


Figure 8. XRD pattern of the $\text{Li}_{6.9}\text{TO}$ -electrolyte coexisting system in C80 high temperature measurements stopped at 185°C (i) and 300°C (ii). Panel (iii) displays the XRD pattern of $\text{Li}_{6.9}\text{TO}$ before the high temperature measurements.

the lithium intercalated in $\text{Li}_{6.9}\text{TO}$,¹ according to:



Since only LiF was observed as the main product of the coexisting system below 185°C, above reactions are the main contribution to peak N1 in Figure 7ii. Li_2CO_3 was found in the product from the calorimetry test stopped at 300°C. It comes from the reaction between the lithium intercalated in LTO and the solvent,¹⁷ which should be the cause of peak N2, as following:



Based on the above analysis, we summarized the thermodynamic and kinetic parameters in Table II and the overall reactions for the $\text{Li}_{6.9}\text{TO}$ -electrolyte coexisting system should be as following:

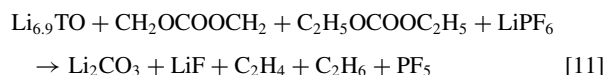


Table II. Thermodynamics and kinetics of $\text{Li}_{6.9}\text{TO}$ and 1.0 M $\text{LiPF}_6/\text{EC} + \text{DEC}$ electrolyte at 2:1 mass ratio from 50.0 to 300.0°C.

$\text{Li}_{6.9}\text{TO}$ -electrolyte 2:1	Associated reaction	Onset temp. (°C)	Peak temp. (°C)	Heat (J g ⁻¹)	Activation energy E (kJ mol ⁻¹)	pre-exponential factor A (s ⁻¹)	Relativity R ²
Peak N1	decomposition of LiPF_6 , reaction of PF_5 and Li intercalated in LTO	100.3	168.2	-306.8	158.7	3.1×10^{16}	0.992
Peak N2	reaction of Li intercalated in LTO and solvents	180.4	206.2	-269.4	549.1	1.2×10^{75}	0.991
Total		—	—	-576.2	—	—	—

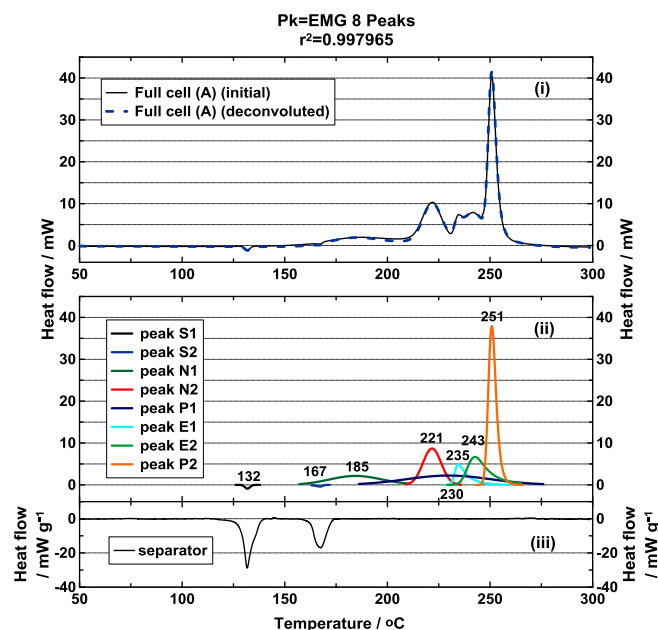


Figure 9. Heat flow versus temperature for the LNCMO/LTO full cell (A) (i), the corresponding thermal peaks obtained from the deconvolution analysis (ii) and the separator (iii).

Thermal behavior of the LNCMO/LTO cell.—The thermal behavior of a full cell (A) contained the same mass of electrode and electrolyte as the above electrode-electrolyte coexisting system was studied by the calorimetry test to determine the thermal stability of LNCMO/LTO full cell based on above analysis. The cell (A) was composed of 118.2 mg $\text{Li}_{0.9}\text{TO}$, 127.6 mg $\text{Li}_{0.41}\text{NCMO}$, 121.3 mg electrolyte, 17.9 mg separator, 23.5 mg aluminum foil and 37.8 mg copper foil.

The solid line in Figure 9i shows the initial heat flow plot of the full cell (A), and displays complex thermal behavior with overlapped peaks. The dotted line in Figure 9i shows the corresponding deconvoluted plot, which was composed of eight peaks S1~P2, as shown in Figure 9ii. In accordance with the previous discussion on the electrode-electrolyte systems, the deconvoluted peaks of the full cell (A) can be distinguished as specific reactions, and the detailed thermal characteristics of each peak were obtained and summarized

in Table III. Given that various types of materials existed in the full cell, it is unreasonable to determine the heat per unit mass of each peak based on the mass of positive or negative electrode or electrolyte. Hence, the heat per unit mass was calculated based on the mass of related material in the following analysis.

Peak S1 and S2 are two endothermic processes with peak temperatures of 131.8 and 167.2°C and heat generation of 845.9 and 587.1 mJ, respectively. We ascribe them to the melting of separator. Corresponding test of separator was performed and the result is shown in Figure 9iii. The separator exhibited two endothermic peaks at 131.7 and 167.4°C with heat generation of 50.2 and 35.8 J g⁻¹, which correspond to the melting process of polyethylene and polypropylene layers. By dividing the heat of peak S1 and S2 in Figure 9ii by the separator mass, we can obtain values of 47.3 and 32.8 J g⁻¹, which approximate to the values obtained from Figure 9iii. Therefore, one can conclude that peaks S1 and S2 are assigned to the melting of separator.

Along with the second melting process of the separator, the full cell (A) began to release heat as shown in peak N1. The heat per unit mass can be specified as 176.6 or 163.6 J g⁻¹ based on the mass of LTO or LNCMO, respectively. It is hard to find a peak resembling peak N1 from the previous discussion. However, the temperature range of peak N1 (158~210°C) coincides with the latter part of the peak N1 in Figure 7ii. The former part of peak N1 might be offset or delayed by the endothermic effect of the separator. If we integrate the heat flow versus time within 160~210°C for peak N1 in Figure 7ii, the heat is specified as 177.9 J g⁻¹, which is similar to that of peak N1 in Figure 9ii. Thus, we ascribe peak N1 in Figure 9ii to the reaction between PF_5 and lithium intercalated in LTO.

Peak N2 occurred from 210.8°C with a peak temperature of 221.2°C. By dividing the heat value by the mass of LTO, the heat per gram was calculated as -254.1 J g⁻¹, which is close to the heat of the peak N2 in Figure 7ii (-269.4 J g⁻¹). This indicates peak N2 in Figure 9ii is caused by the reaction between lithium intercalated in LTO and solvent. Peak P1 released heat from 186.5°C and reached its maximum at 229.3°C. If the heat is divided by the mass of LNCMO, the heat per gram is obtained as -311.5 J g⁻¹, which compares well with that of peak (a) in Figure 5ii (-308.9 J g⁻¹). Therefore, peak P1 is assigned to the partial decomposition of LNCMO.

With the increase in temperature, peaks E1 and E2 show exothermic behavior. In comparison with peaks in Figure 5ii and Figure 7ii, it seems that no parallel peaks can be found for peaks E1 or E2. Nonetheless, we checked the exothermic peaks of the electrolyte in our previous work,¹⁷ and found that they compare well with peaks E1 and E2 in Figure 9ii. The heat generation of the two exothermic peaks of the electrolyte were -114.0 and -243.8 J g⁻¹.¹⁷ They are close to

Table III. Thermodynamics and kinetics of LNCMO/LTO full cell (A) from 50.0 to 300.0°C.

	Associated reaction	Onset temp. (°C)	Peak temp. (°C)	Heat (mJ)	Heat per gram* (J g ⁻¹)	Activation energy E (kJ mol ⁻¹)	pre-exponential factor A (s ⁻¹)	Relativity R ²
Peak S1	melting of separator	129.4	131.8	845.9	47.3	—	—	—
Peak S2		165.6	167.2	587.1	32.8	—	—	—
Peak N1	reaction of PF_5 and Li intercalated in LTO	158.3	184.5	-20870.9	-176.6	171.7	6.2×10^{19}	0.982
Peak N2	reaction of Li intercalated in LTO and solvents	210.8	221.2	-30031.4	-254.1	665.4	1.1×10^{80}	0.987
Peak P1	partial decomposition of LNCMO	186.5	229.8	-39742.8	-311.5	193.9	7.5×10^{15}	0.983
Peak E1	reaction of salt and solvents	228.1	234.5	-13493.9	-111.2	998.7	2.2×10^{88}	0.988
Peak E2		232.7	242.7	-26733.3	-220.4	756.7	7.2×10^{93}	0.980
Peak P2	decomposition of LNCMO, oxidization of solvents	246.2	250.9	-52630.8	-412.5	492.4	9.1×10^{121}	0.991
Total		—	—	-182070.1	—	—	—	—

*Heat generation based on specific electrode.

the heats of peaks E1 and E2 (-111.2 and 220.4 J g^{-1}), which were determined by dividing the heat by the mass of electrolyte. It should be noted that the activation energy of the reaction between electrolyte and electrode is lower than that of the separate electrolyte obtained in Ref. 17. Accordingly, the electrolyte reacts with the electrode first. Then, if there is enough electrolyte present in the system, the electrolyte might follow the reactions between the solvents and lithium salt and release heat, resulting in peaks E1 and E2 in Figure 9ii.

After above peaks, a sharp peak shown as peak P2 appeared with a peak temperature of 250.9°C . Based on the mass of LNCMO, the heat per unit mass of peak P2 can be identified as -412.5 J g^{-1} , which is close to the heat of peak P2 (-395.7 J g^{-1}) shown in Figure 5ii. However, peak P2 in Figure 9ii shows lower onset and peak temperatures and lower activation energy in contrast with peak P2 in Figure 5ii. We believe that the oxidation of solvents might occur more easily and thoroughly, affected by the heat generated by the previous peaks E1 and E2. Consequently, peak P2 is the result of the complete decomposition of LNCMO and the oxidation of the solvent.

From the above analysis, it can be found that the thermal behavior of the full cell can be divided into different stages with elevated temperature. The released heat above 245°C occupies the largest fraction in the total heat generation. The decomposition of LNCMO and the following oxidation of solvent could be the main reason for the thermal runaway of a LNCMO/LTO cell.

One thing that should be noted is that the amount of the electrolyte used in the full cell (A) is higher than that of the commercial cell, which is apt for the study on the interaction between the electrodes and the electrolyte.²¹ Moreover, for the sake of understanding thermal stability of a commercial LNCMO/LTO cell at high temperature, the calorimetry test of full cell (B) was performed. It consisted of $122.5 \text{ mg Li}_{6.9}\text{TO}$, $130.1 \text{ mg Li}_{0.41}\text{NCMO}$, $62.4 \text{ mg electrolyte}$, $18.2 \text{ mg separator}$, $23.5 \text{ mg aluminum foil}$ and $37.8 \text{ mg copper foil}$. Its mass distribution is close to the commercial LNCMO/LTO battery. Figure 10i shows the heat flow plot of full cell (B) at high temperature. The heat flow plot of full cell (A) is shown as a red dotted line for comparison. The full cell B is thermally stable below 170°C with a $0.2^\circ\text{C min}^{-1}$ heating rate. Then, the cell released heat gently within $175\sim 220^\circ\text{C}$ and exhibited an evident exothermic peak with a peak temperature of 230°C . The heat generation throughout the entire measurement was -95452.6 mJ . It is clear that the thermal behavior of full cell (B) is simpler than that of full cell (A).

Figure 10ii shows the deconvoluted thermal peaks S1~NP and their thermodynamic and kinetic parameters were summarized in Table IV. The heat per unit mass of each peak was also determined by dividing the heat by the mass of the involved material. Peaks S1 and S2 displayed endothermic behavior with peak temperatures of 131.5 and 167.3°C , which result from the separator melting. Judging from

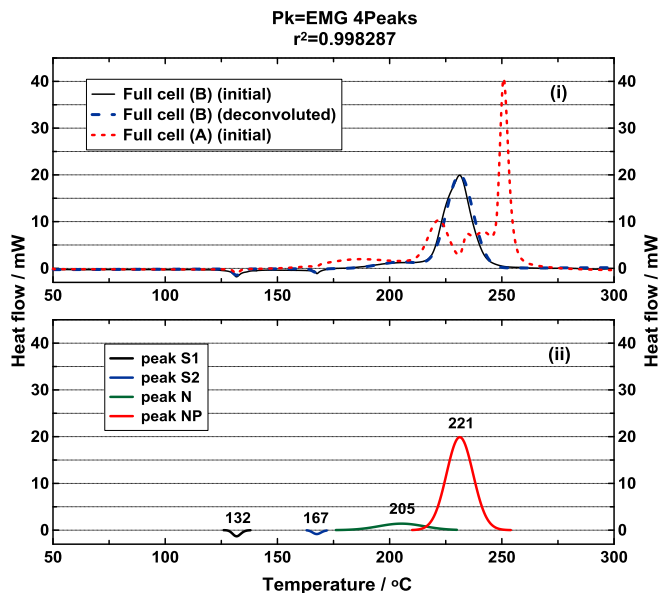


Figure 10. Heat flow versus temperature for the LNCMO/LTO full cell (B) (i), the corresponding thermal peaks obtained from the deconvolution analysis (ii).

the peak shape and the temperature ranges as well as kinetic parameters listed in Table III and Table IV, peak N in Figure 10ii is believed to be a combination of peaks N1 and P1 in Figure 9ii. Nevertheless, the heat per unit mass of peak N is -81.6 or -86.6 J g^{-1} by dividing the heat by the mass of LNCMO or LTO, which is lower than the values of peak N1 or P1 in Figure 9ii. On account of the reduction in the electrolyte mass, the reactivity between the lithium intercalated in LTO and the electrolyte might decrease, resulting in a lower heat generation.

Peak NP appeared from 210 to 254°C while four peaks (peaks N2, E1, E2 and P2) occurred within a similar temperature range in Figure 9ii. Because there is less electrolyte available in full cell (B), peaks E1 and E2 in Figure 9ii that resulted from the electrolyte should not be the cause for peak NP in Figure 10ii. If we divide the heat of peak NP by the mass of the LNCMO or LTO, either of values (-687.4 or -730.1 J g^{-1}) is close to the sum (-666.6 J g^{-1}) of the heat of peak N2 and P2 (-254.1 and -412.5 J g^{-1}) in Figure 9ii. Consequently, the broad peak NP in Figure 10ii is related to reactions between the solvents and the lithium intercalated in Li_xTO , the decomposition of Li_xNCMO and the oxidation of the solvents.

Table IV. Thermodynamics and kinetics of LNCMO/LTO full cell (B) from 50.0 to 300.0°C .

	Associated reaction	Onset temp. ($^\circ\text{C}$)	Peak temp. ($^\circ\text{C}$)	Heat (mJ)	Heat per gram* (J g^{-1})	Activation energy E (kJ mol^{-1})	pre-exponential factor A (s^{-1})	Relativity R^2
Peak S1	melting of separator	129.4	131.5	872.6	47.9	—	—	—
Peak S2		165.6	167.3	592.7	32.6	—	—	—
Peak N	reaction of Li intercalated in LTO and electrolyte	176.0	205.3	-10610.5	$-(86.6\sim 81.6)$	$186.1\sim 195.3$	9.7×10^{17} $\sim 1.1 \times 10^{18}$	0.991
Peak NP	reaction of Li intercalated in LTO and solvents, decomposition of LNCMO, oxidation of solvents	210.8	221.2	-30031.4	$-(730.1\sim 687.4)$	$500.6\sim 512.7$	4.3×10^{87} $\sim 8.9 \times 10^{87}$	0.988
Total		—	—	-39176.6	—	—	—	—

*Heat generation based on specific electrode.

Generally, only one main exothermic peak can be observed for the LNCMO/LTO full cell when the temperature is above 210°C if the mass ratio of the full cell shows the same pattern as the commercial cell. This is different from the full cell system with more electrolyte (full cell (A)), where the thermal behavior can be characterized by obvious stages from 50 to 300°C. Nonetheless, the main contribution to the heat generation for both of the two full cells is caused by the reactions between solvents and positive electrodes.

Conclusions

Electrochemical and thermal behavior of LNCMO, LTO half cells and LNCMO/LTO full cells at high temperature were analyzed in this work. Both of LNCMO and LTO half cells displayed outstanding electrochemical performance at normal and high temperature. The LNCMO/LTO full cells cycled at 25 and 60°C under a C/2 rate exhibited 96.9% and 95.3% capacity retention, and both showed more than 99% CE over 100 cycles. Furthermore, the full cell showed as high as 91.6% and 84.9% capacity retention even when cycled under a 5C rate at 25 and 60°C, respectively. The remarkable rate capability and cycling behavior indicate promising electrochemical performance of the LNCMO/LTO full cells not only at room temperature but also at temperatures up to 60°C.

Based on the calorimetry measurements and deconvolution as well as XRD analysis, thermal reactions occurring in the electrode-electrolyte coexisting system were determined. The corresponding thermodynamic and kinetic characteristics of these reactions were also specified. According to these results, detailed analysis on the LNCMO/LTO full cells were performed. The full cell system underwent various periods arising from different thermal reactions with the increase of the temperature: the melting of the separator, the reaction between PF₅ and the lithium intercalated in LTO, the reaction between solvents and the lithium intercalated in LTO, partial decomposition of LNCMO, the reaction between PF₅ and solvents, complete decomposition of LNCMO and the oxidization of solvents. These reactions overlap with each other and make the thermal behavior of the full cell complex at elevated temperature. On the other hand, the thermal study of the full cell with similar proportions to the commercial full cell showed a simpler thermal behavior from 50 to 300°C and reduced heat generation. Despite the difference, the full cell similar to the commercial one showed important thermal properties in common with the full cell with more electrolyte: the systems are thermally stable below 150°C, indicating a good thermal stability of the LNCMO/LTO system; the heat generated by the reactions between the solvents and LNCMO is the first contribution to the heat generation, and the second contribution is ascribed to the reactions between the solvents and LTO, implying that decreasing the reactivity of the LNCMO in the

presence of the solvents should be an effective way to further improve the thermal stability of the LNCMO/LTO chemistry.

Acknowledgments

This work is supported by the National Natural Science Foundation of China (No. 51504282 and No. 51176183) and the Shandong Provincial Natural Science Foundation (No. ZR2014EEQ036). The authors also acknowledge the financial support of the Opening Fund of State Key Laboratory of Fire Science of University of Science and Technology of China (No. HZ2015-KF14), the External Cooperation Program of BIC, CAS (No. 211134KYSB20150004) and the Fundamental Research Funds for the Central Universities (No. 15CX02018A and No. WK2320000034). Dr. Q.S. Wang is supported by Youth Innovation Promotion Association CAS (No.2013286).

References

1. J. Jiang, J. Chen, and J. Dahn, *J. Electrochem. Soc.*, **151**(12), A2082 (2004).
2. K. Mukai, Y. Kato, and H. Nakano, *J. Phys. Chem. C*, **118**(6), 2992 (2014).
3. T. Ohzuku, A. Ueda, and N. Yamamoto, *J. Electrochem. Soc.*, **142**(5), 1431 (1995).
4. A. Devie, M. Dubarry, and B. Y. Liaw, *J. Electrochem. Soc.*, **162**(6), A1033 (2015).
5. K. Amine, I. Belharouak, Z. Chen, T. Tran, H. Yumoto, N. Ota, S. T. Myung, and Y. K. Sun, *Adv. Mater.*, **22**(28), 3052 (2010).
6. S. K. Martha, O. Haik, V. Borgel, E. Zinigrad, I. Exnar, T. Drezen, J. H. Miners, and D. Aurbach, *J. Electrochem. Soc.*, **158**(7), A790 (2011).
7. N. Schweikert, R. Heinzmann, A. Eichhöfer, H. Hahn, and S. Indris, *Solid State Ion.*, **226** 15 (2012).
8. N. Takami, H. Inagaki, T. Kishi, Y. Harada, Y. Fujita, and K. Hoshina, *J. Electrochem. Soc.*, **156**(2), A128 (2009).
9. H. Wu, I. Belharouak, H. Deng, A. Abouimrane, Y.-K. Sun, and K. Amine, *J. Electrochem. Soc.*, **156**(12), A1047 (2009).
10. K. Zaghib, M. Dontigny, A. Guerfi, J. Trottier, J. Hamel-Paquet, V. Gariépy, K. Galoutov, P. Hovington, A. Mauger, and H. Groult, *J. Power Sources*, **216**, 192 (2012).
11. M. Ecker, N. Nieto, S. Käbitz, J. Schmalstieg, H. Blanke, A. Warnecke, and D. U. Sauer, *J. Power Sources*, **248**, 839 (2014).
12. J. Vazquez-Arenas, L. E. Gimenez, M. Fowler, T. Han, and S.-k. Chen, *Energy Convers. Manage.*, **87**, 472 (2014).
13. J. Belt, V. Utgikar, and I. Bloom, *J. Power Sources*, **196**(23), 10213 (2011).
14. A. Mahmoud, I. Saadoun, J. M. Amarilla, and R. Hakkou, *Electrochim. Acta*, **56**(11), 4081 (2011).
15. F. Zhou, X. Zhao, A. van Bommel, X. Xia, and J. Dahn, *J. Electrochem. Soc.*, **158**(2), A187 (2011).
16. N. Takami, H. Inagaki, Y. Tatebayashi, H. Saruwatari, K. Honda, and S. Egusa, *J. Power Sources*, **244**, 469 (2013).
17. P. Ping, Q. Wang, P. Huang, J. Sun, and C. Chen, *Appl. Energy*, **129**, 261 (2014).
18. R. A. Dunlap, D. A. Small, D. D. MacNeil, M. N. Obrovac, and J. R. Dahn, *J. Alloys Compd.*, **289**(1–2), 135 (1999).
19. I. Belharouak, W. Lu, D. Vissers, and K. Amine, *Electrochem. Commun.*, **8**(2), 329 (2006).
20. P. Röder, N. Baba, and H.-D. Wiemhöfer, *J. Power Sources*, **248**, 978 (2014).
21. M. Koltypin, D. Aurbach, L. Nazar, and B. Ellis, *Electrochem. Solid-State Lett.*, **10**(2), A40 (2007).